

# Toward a Robust, Higher-Order Cut-Cell Method for Viscous Flows

James M. Modisette\* and David L. Darmofal†

*Aerospace Computational Design Laboratory, Massachusetts Institute of Technology*

In this paper, a cut-cell method is considered in which (1) the background mesh is composed of simplices allowing arbitrary anisotropy and (2) a higher-order discontinuous Galerkin (DG) discretization is applied. This paper quantifies the impact of three limitations of this simplex cut-cell technique, specifically: the presence of small volume ratios (i.e. cut elements with volume that is arbitrarily small compared to the volume of its neighboring elements); the application of integration rules designed for arbitrarily cut elements; and, the use of a Cartesian solution space. Solutions to these issues are presented and the paper concludes by demonstrating the two-dimensional cut-cell method with simulations of high Reynolds number RANS flow over a complex geometry.

## I. Introduction

Computational Fluid Dynamics (CFD) has become an essential tool for modeling and design in many communities including the aerospace industry. Unfortunately, CFD is still hindered by an inability to robustly generate flow solutions on complex geometries without human involvement. An approach that can potentially reduce this human involvement is output-based mesh adaptation which generates a series of meshes in an automated manner with the objective of minimizing the error of an engineering output.<sup>1,2</sup> Engineering applications of output-based adaptation include outputs of lift and drag for two-dimensional and three-dimensional flows,<sup>3-5</sup> sonic problems,<sup>6,7</sup> and forces on re-entry vehicles.<sup>8</sup> There are two requirements for performing output-based adaptation. The first is the solution of an adjoint problem, where the adjoint relates the error in an output of interest to the local residual. The adjoint problem requires the solution of a linearized system of equations that is the same size as the discretized system for the flow equations. The second requirement for automated output-based adaptation is robust mesh generation.

Cart3D, a three-dimensional Cartesian solver for the Euler equations,<sup>9</sup> is a prime example of the benefits of robust mesh generation to a flow solver. Cart3D is based on embedding boundaries into Cartesian quadrilateral background meshes and has been proven capable of handling very complex geometries like in the space shuttle debris calculations performed by Murman et al.<sup>10</sup> Work by Nemeč<sup>8,11,12</sup> has added adjoint-based error estimate and adaptive refinement. However, a Cartesian quadrilateral mesh approach limits the directions of anisotropy that are achievable, making the discretization of arbitrarily-oriented shock waves, boundary layers, or wakes highly inefficient. The simplex cut-cell method, presented by Fidkowski and Darmofal,<sup>13-15</sup> presents an autonomous route for generating computational meshes with high anisotropy. Combining the simplex cut-cell method with a higher-order discretization, like the discontinuous Galerkin (DG) method<sup>16-21</sup> used in this work, provides the necessary tools to solve viscous flows over complex geometries.

Fidkowski demonstrated the ability of the simplex cut-cell method to solve Euler and Navier-Stokes flows in two dimensions and Euler flows in three dimensions. The method was also used<sup>22</sup> to model a rotor in hover. This paper quantifies the impact of three limitations of this simplex cut-cell technique, specifically: the presence of small volume ratios (i.e. cut elements with volume that is arbitrarily small compared to the volume of its neighboring elements); the application of integration rules designed for arbitrarily cut elements; and, the use of a Cartesian solution space on each element. Solutions to these issues are presented and the paper concludes by demonstrating the two-dimensional cut-cell method with simulations of high Reynolds number RANS flow over a complex geometry.

\*Doctoral candidate, 77 Massachusetts Ave. 37-435, Cambridge, MA, 02139, jmmodi@mit.edu

†Associate Professor, AIAA Associate Fellow, 77 Massachusetts Ave. 333-207, Cambridge, MA, 02139, darmofal@mit.edu

## II. Small Volume Ratios

In the cut-cell method small volume ratios occur when an arbitrarily small cut element is next to a neighbor of normal size as shown in Figure 1. Small volume ratios have two detrimental results. First, small volume ratios result in oscillations of boundary distributions along a cut boundary, as shown in Figure 2. The oscillations due to small volume ratios are not necessarily diminished with mesh refinement. The second impact of small volume ratios is poor conditioning of the linear system in the Newton solver.

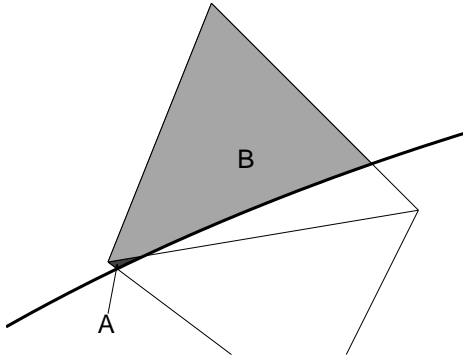


Figure 1. Example of a small volume ratio. Typically small volume ratios occur when a grid node is kept just inside the computational domain by the cut-cell intersection problem.

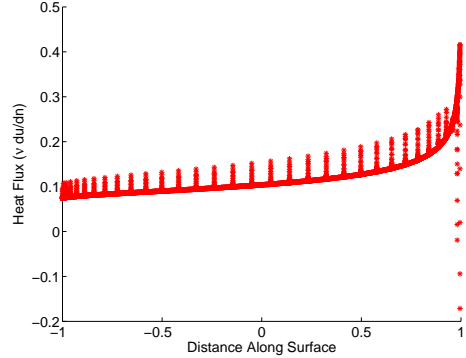


Figure 2. Plot of the heat flux distribution along the surface for a two-dimensional convection-diffusion problem. The distribution illustrates the jumps in the heat flux distribution along the surface which result from elements with small volume ratios.

To study the impacts of elements with small volume ratios, a one-dimensional reaction-diffusion problem is introduced. Specifically the problem is

$$u - \nu \nabla^2 u = f(x), \quad (1)$$

where  $\nu > 0$  and the exact solution,  $u_e(x) = \sin(2\pi x) - x + 1$ , is not in the polynomial solution space of the DG discretization. The volume ratio is defined as

$$\text{VR}_i = \frac{\text{length}_i}{\max_{j=\text{neighbor}} (\text{length}_j)}$$

and the model domain has uniformly sized elements with one small element on the left boundary as shown in Figure 3. Thus, the critical volume ratio for the model problem is

$$\text{VR}_1 = \frac{\text{length}_1}{\text{length}_2}.$$



Figure 3. Diagram of domain for the 1D model problem. The domain has uniformly spaced elements with a single small element on the left domain boundary.

Volume Ratio	1	$1 \times 10^{-3}$	$1 \times 10^{-6}$	$1 \times 10^{-9}$	$1 \times 10^{-12}$
Residual Decrease Factor	$4 \times 10^{14}$	$1 \times 10^{11}$	$3 \times 10^8$	$2 \times 10^5$	$2 \times 10^2$

Table 1. Relative “convergence” of the residual for the one-dimensional reaction diffusion problem over varying volume ratios, using a direct solver. Demonstrates the poor convergence of the linear problem as the volume ratios get small.

Table 1 illustrates the poor convergence of the residual in the linear problem solved with a direct solver as the volume ratio gets smaller. With a volume ratio on the  $\mathcal{O}(10^{-10})$ , the residual only decreases by

$\mathcal{O}(10^{-2})$ . The impact of the small volume ratio can affect the entire solution procedure for a non-linear solver. The solver struggles to effectively update the solution in the small element and drive the residual to zero. The impact of the small volume ratios can be further illustrated by looking at the condition number of the stiffness matrix for the one-dimensional model problem. Figure 4(a) shows the variation in the condition number of the stiffness matrix versus  $h$  (the element size of all but the left most element in the model domain). As it should for a diffusion problem the condition number scales with  $\mathcal{O}(h^{-2})$  for a fixed volume ratio. However, the volume ratio has a significant impact on the condition number of the stiffness matrix. Figure 4(b) shows that the condition number also scales with  $\mathcal{O}(VR^{-1})$ .

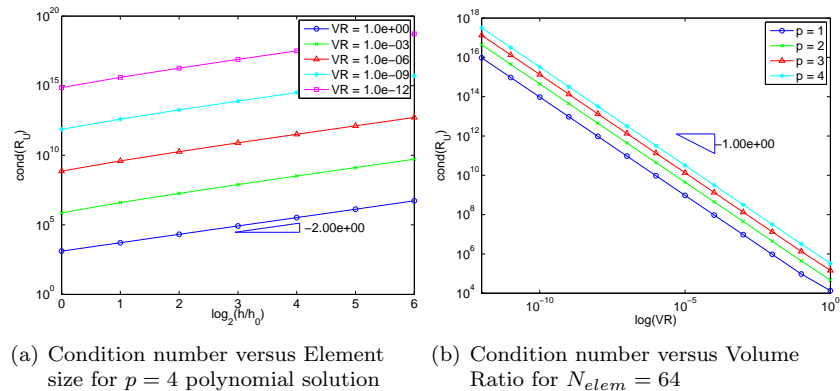


Figure 4. Plot showing the variation of the condition number versus element size and volume ratio.

Small volume ratios adversely affect the condition number of the linear system resulting from the DG discretization and stalls convergence of a non-linear system of equations in many cases. The  $L^2$  error,  $\|u - u_h\|_{L^2}$ , of the solution is largely unaffected. Figure 5 shows the  $L^2$  error convergence at different critical volume ratios and polynomial solution orders with only small changes evident due to volume ratio.

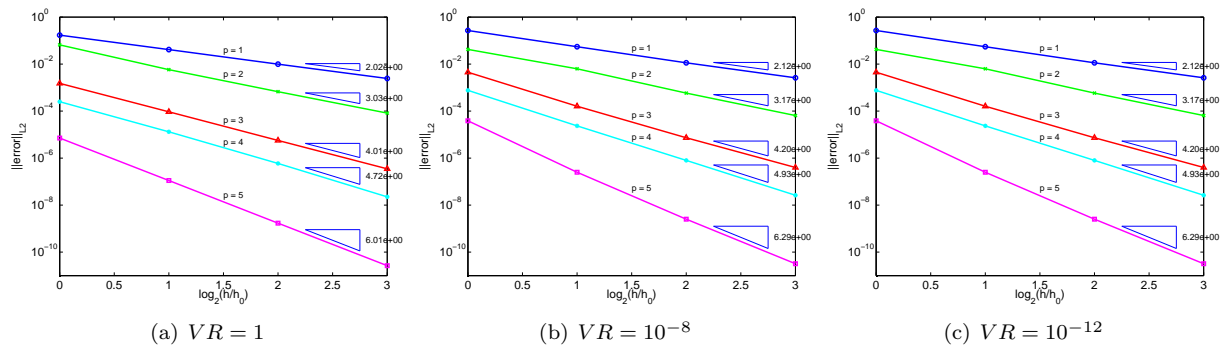
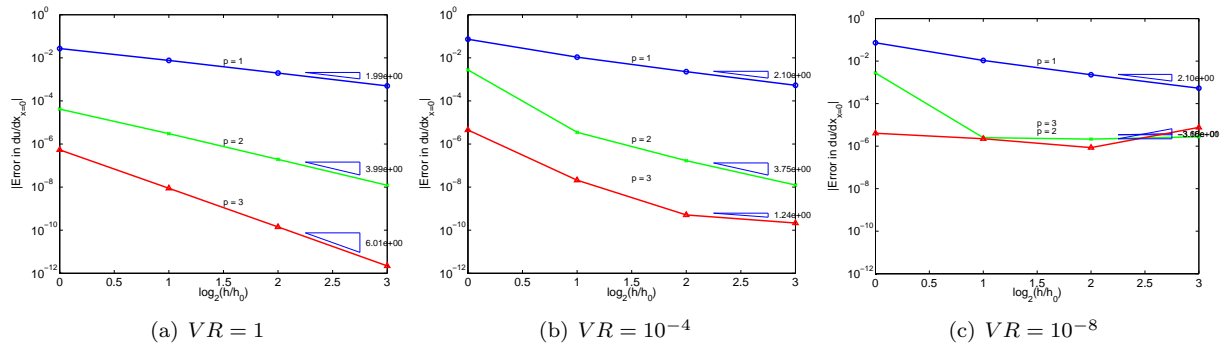


Figure 5. Plots showing the convergence of the  $L^2$  solution error with varying critical volume ratio. Due to the tiny size of the element with the critical volume ratio it has no impact on the  $L^2$  error.

Although the  $L^2$  error is unaffected, the derivative at the boundary has strong dependence on the volume ratio. Figure 6 shows that even at volume ratios of  $\mathcal{O}(10^{-4})$ , where the volume ratio had a much smaller impact on the condition number of the linear system, the error in the boundary output,  $\left. \frac{du}{dx} \right|_{x=0}$ , is significant and cannot be neglected. The small volume ratios eliminate all the benefits of the higher-order DG discretization.

A few ideas were considered to handle the small volume ratio case. A possibility is to nudge all the problem nodes, grid nodes located in the computational domain but close to the embedded surface, outside of the computational domain or onto the embedded surface. By nudging the problem nodes, the typical grid typology which results in small volume ratios would be eliminated. The method of grid node nudging has been used in two dimensions with some success, but as the geometry becomes more complex and the cut-cell



**Figure 6.** Plots showing the convergence, or lack there of, of the error in the output  $\frac{du}{dx}|_{x=0}$  for a range of volume ratios. The error in boundary quantity output immediately feels the impact of small volume ratios.

method is extended to three dimensions the direction in which to nudge the nodes becomes a more difficult problem. In order to maintain an algorithm which is extendable to three dimensions, small volume ratios are eliminated by merging, following the work of<sup>23,24</sup>

Essentially, because the elements with small volume ratios are so small in comparison to the neighbors, solution quality is not affected if the small elements are just merged into their neighbor sharing the largest common face. The common face between the large and small neighbor is eliminated and the integration rules for the small element and its other non-common faces are just added to the larger neighbor. The basis used to represent the polynomial solution remains the basis originating from the larger element.

Once merging is used, the linear system no longer suffers from the volume ratio penalty to its condition number and the boundary outputs recover their optimal convergence properties. Figure 7 shows the convergence of the error in  $\frac{du}{dx}|_{x=0}$  at the extremes of the critical volume ratio. Figure 7 clearly shows that, whether the volume ratio is 1 or  $10^{-10}$ , merging allows for optimal convergence of the boundary output.

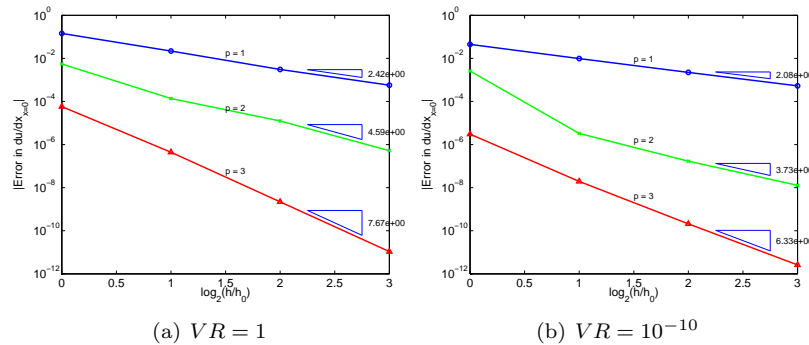


**Figure 7.** Plots showing the improvement in the convergence of the boundary output,  $\frac{du}{dx}|_{x=0}$ , when merging is used in the 1D model problem.

Merging is also tested on a two-dimensional convection-diffusion problem of the form

$$\vec{V} \cdot \nabla u - \frac{1}{Pe} \nabla^2 u = S, \quad (2)$$

with a vortex flow velocity field,  $V_\theta = \frac{1}{r}$  and the exact solution,  $u_e = 1 - \exp\left(\frac{-(r-R)}{\sqrt{\frac{c\theta r}{Pe}}}\right)$ . A relatively low Peclet number flow,  $Pe = 100$ , is used to limit the necessary anisotropy of the meshes to an aspect ratio of 10. Figure 8 shows a model of the domain. To measure solution error the heat flux distribution error, defined as  $\sqrt{\int_{S_bf} (\nu \frac{\partial u}{\partial n} - \nu \frac{\partial u_e}{\partial n})^2 dS}$ , is used. The heat flux distribution error is sensitive to oscillations in the heat flux distribution which is important for the assessment of solution quality in the presence of small volume ratios.

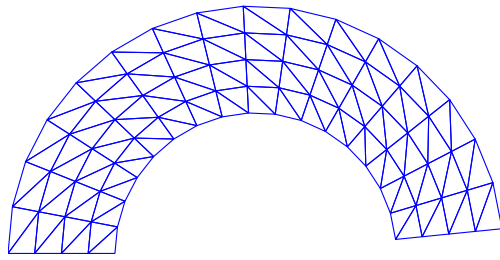


Figure 8. An example domain used with the two-dimensional scalar convection-diffusion model problem. For viewing the aspect ratio has been set to 1. Also included are images of the globally curved mesh (b) and the boundary curved mesh (c).

To set up cut-cell meshes with small volume ratios the structured background mesh, shown in Figure 8, is stretched radially inward by 99.9% of the radial element spacing leaving the outer boundary location unchanged. The radial stretching leaves a grid node barely inside the computational domain. When the background mesh is cut volume ratios on the order of  $10^{-6}$  are created. For two-dimensional grids merging continues one internal face at a time until the global minimum volume ratio is above a set tolerance. The volume ratio tolerance used in this work is  $10^{-2}$ .

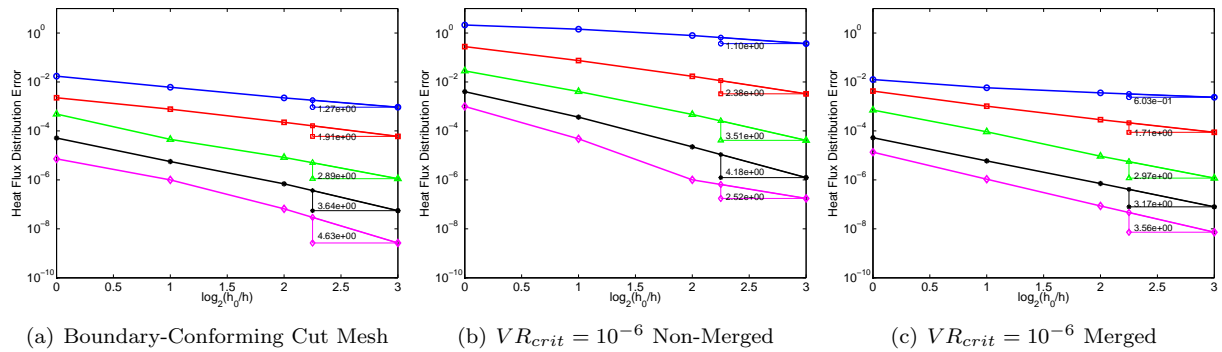


Figure 9. Convergence of the heat flux distribution error for cut-cell meshes. The errors in boundary-conforming cut cases are compared to the errors in cut meshes with small volume ratios that have either been merged out or remain.

Figure 9 shows the convergence history of the heat flux distribution error for three different cut-cell grids. The first will be referred to as a boundary-conforming cut grid as it is a globally linear background mesh with a higher-order embedded surface that exactly intersects the background grid nodes on the boundary. The resulting cut elements have two linear faces and one curved face. The other two grids studied are the merged and non-merged version of the  $VR = 10^{-6}$  cut grids. The merged and non-merged results have very different convergence trends. The cut grids with small volume ratios and no merging have a large heat flux distribution penalty added to them, but the rate at which they converge is still close to optimal. When merging, the initial heat flux distribution error is approximately the same for the merged mesh and the boundary-conforming cut mesh, but the rates for the merged mesh are not optimal. Currently, there is not a satisfactory explanation for why the merged mesh has such low convergence rates, but what is clear is that the merged mesh has lower heat flux distribution errors and higher accuracy than the non-merged mesh. The importance of merging becomes even clearer in Figure 10, where the heat flux distribution itself is plotted over the range of grid refinements (across) and solution orders (down). As the mesh is refined and the solution order is increased, even without merging, the heat flux distribution improves. In fact, highly resolved meshes with higher-order solutions (bottom right in Figure 10) do not show oscillatory behavior. However, in the under-resolved meshes there is a huge penalty in the heat flux distribution when merging is not used. In the context of an adaptive method a larger loss of accuracy in under-resolved meshes is particularly troublesome.

Along with boundary distribution data, the other critical reason for merging is the condition number

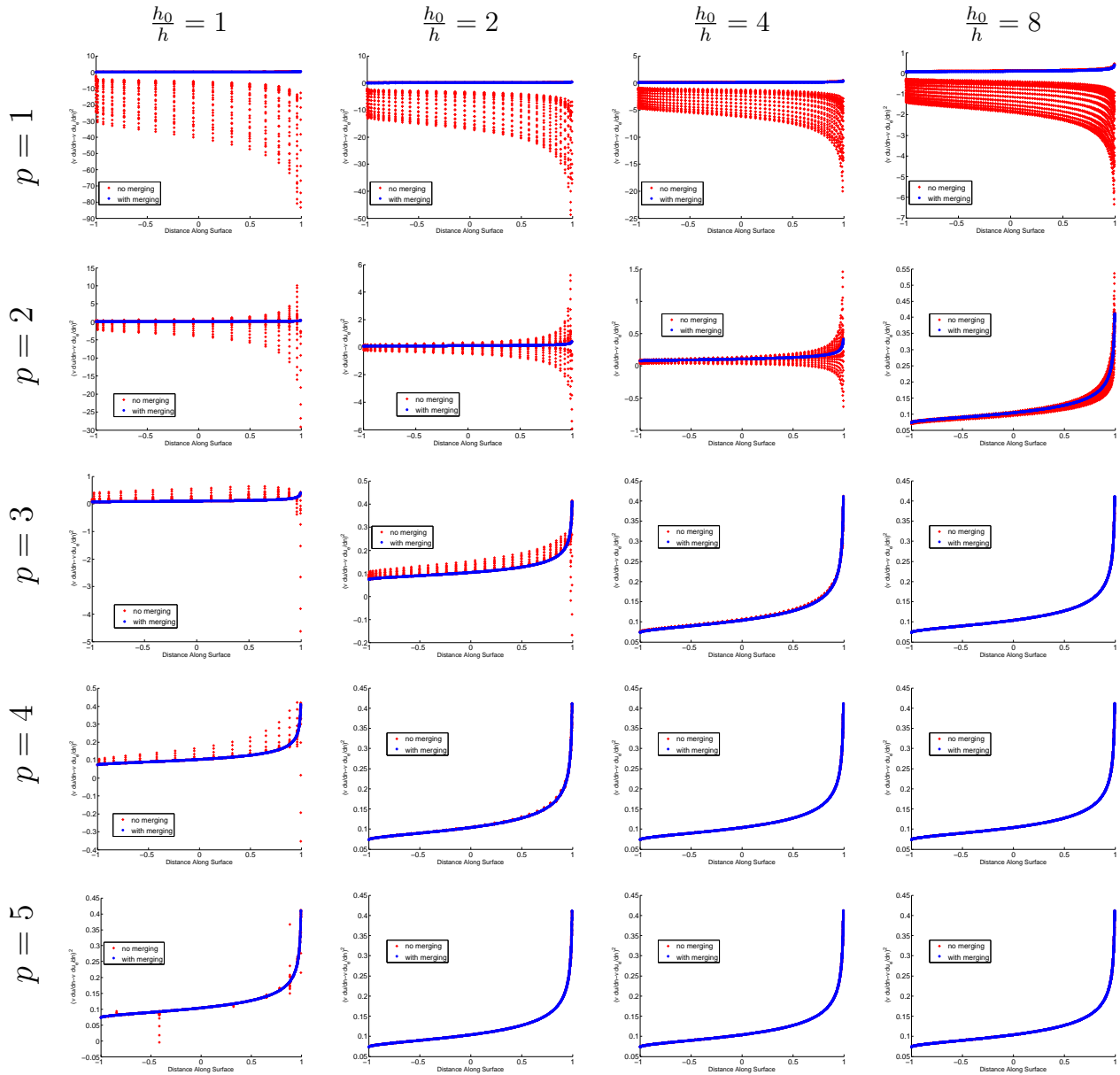


Figure 10. Boundary distributions of heat flux for the two-dimensional convection-diffusion problem using the merged and non-merged cut grids. The boundary distributions highlight the importance of merging particularly in cases with under-resolved meshes.

of the linear system when small volume ratios exist. Table 2 lists the GMRES iteration count and drop in the residual after one linear solver for the merged and non-merged cut meshes. The linear system is solved using left preconditioned ILU(0).<sup>25</sup> In the linear system solve the preconditioned residual always drops by at least  $10^{14}$  in the number of GMRES iterations listed. The residual drop is included in Table 2 to illustrate the difference between the preconditioned residual and the residual itself. For the non-merged high-order solution cases, Table 2(a), the drop in the residual has little correspondence with the drop in the preconditioned residual due to the large condition number of the linear system. The result is that even for the linear convection-diffusion problem multiple linear solves are needed to converge the residual in non-merged meshes. When merging is used, Table 2(b), the drop in the residual is almost constant across the range of mesh refinements and solution orders.

(a) No Merging

	$\frac{h_0}{h} = 1$	$\frac{h_0}{h} = 2$	$\frac{h_0}{h} = 4$	$\frac{h_0}{h} = 8$
p = 1	46 ( $8 \times 10^{14}$ )	136 ( $1 \times 10^{15}$ )	449 ( $1 \times 10^{15}$ )	766 ( $1 \times 10^{15}$ )
p = 2	42 ( $2 \times 10^{14}$ )	112 ( $1 \times 10^{14}$ )	485 ( $1 \times 10^{14}$ )	786 ( $1 \times 10^{14}$ )
p = 3	49 ( $2 \times 10^{12}$ )	156 ( $1 \times 10^{11}$ )	456 ( $7 \times 10^{11}$ )	862 ( $1 \times 10^{12}$ )
p = 4	45 ( $6 \times 10^9$ )	146 ( $2 \times 10^9$ )	590 ( $2 \times 10^9$ )	855 ( $3 \times 10^9$ )
p = 5	49 ( $3 \times 10^7$ )	181 ( $9 \times 10^6$ )	481 ( $7 \times 10^6$ )	833 ( $5 \times 10^6$ )

(b) With Merging

	$\frac{h_0}{h} = 1$	$\frac{h_0}{h} = 2$	$\frac{h_0}{h} = 4$	$\frac{h_0}{h} = 8$
p = 1	49 ( $9 \times 10^{14}$ )	138 ( $7 \times 10^{14}$ )	447 ( $5 \times 10^{14}$ )	853 ( $4 \times 10^{14}$ )
p = 2	43 ( $3 \times 10^{14}$ )	113 ( $8 \times 10^{14}$ )	441 ( $5 \times 10^{14}$ )	792 ( $3 \times 10^{14}$ )
p = 3	52 ( $1 \times 10^{15}$ )	153 ( $6 \times 10^{14}$ )	464 ( $4 \times 10^{14}$ )	793 ( $2 \times 10^{14}$ )
p = 4	46 ( $6 \times 10^{14}$ )	149 ( $5 \times 10^{14}$ )	467 ( $4 \times 10^{14}$ )	842 ( $2 \times 10^{14}$ )
p = 5	51 ( $8 \times 10^{13}$ )	199 ( $1 \times 10^{14}$ )	578 ( $2 \times 10^{14}$ )	868 ( $2 \times 10^{14}$ )

**Table 2.** The GMRES iteration counts and the drop in the residual of the linear system solve for the merged and non-merged meshes that originally had small volume ratios. The GMRES iteration count is the total number of inner GMRES iterations used with GMRES restart after 50 inner iterations.

### III. Integration Rules for Arbitrary Element Shapes

Discontinuous Galerkin finite element discretizations do not require specific element shapes. Only a basis to represent the solution and a set of integration rules within each element are necessary. To include cut cells in a DG discretization a technique to integrate over arbitrary shapes is needed. One possible approach for generating integration rules is to subdivide each cut element into a set of possibly-curved triangles. Though this approach would provide an optimal set of quadrature rules for integration in each element, it cycles back to the original problem of meshing with curved boundaries. For that reason, a more general approach is selected for cut cells.

The method used for integrating over cut elements is to “speckle” sampling points in the cut element and then apply the divergence theorem to compute the integration weights associated with each point such that  $\int_{\Omega} f(\mathbf{x})d\Omega \approx \sum_{q=1}^{N_{quadr}} w_q f(\mathbf{x}_q)$ . Further details can be found in.<sup>13–15,22</sup>

The general method used for generating quadrature-like sums for integration rules has proven to be sufficient for 2D cut-cell cases, but a very large number of quadrature points, upwards of 400 for element area integration, are necessary for  $p = 5$  cases. An example set of points is shown in Figure 11(a). Since the quadrature points are stored and the solution must be sampled at each one during integration, there is a significant added computational cost.

Currently the “speckling” is performed by first randomly selecting a point along the surface of the element boundary, inwardly projecting rays (randomly  $\pm 15^\circ$  off inward normal) from that point, and then randomly selecting a point along the ray between where it enters the domain and where it exits the domain. The reason for such a large number of sampling points is to guarantee coverage of the entire region of an arbitrarily cut element.

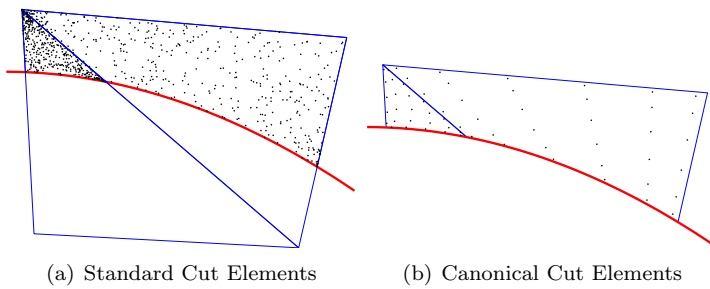


Figure 11. (a) An example of the “speckled” 2D integration points for a cut-cell mesh. In order to support  $p = 5$  solutions upwards of 400 points are necessary to adequately cover the interior of the element. (b) Example of the same cut elements converted to canonical elements.

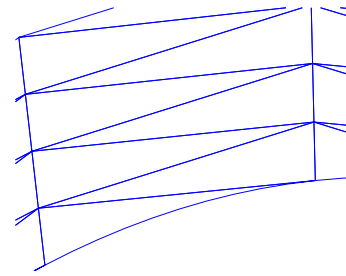


Figure 12. Example of a boundary-curved domain. The boundary-conforming domain is globally linear with a single curved boundary on the geometry surface.

To explore the solution dependence on the randomness in the quadrature rules, the boundary-curved mesh, Figure 12, is used. The selection of this particular grid topology allows the integration procedure to be isolated. Figure 13 shows the convergence history of the heat flux distribution error, where at each solution order and grid refinement level, 100 different sets of randomly “speckled” points are used for integration rules. For each polynomial order the convergence of the minimum and maximum heat flux distribution errors are plotted versus grid refinement. For solution orders  $p = 1$  through  $p = 4$  there is no variation in the convergence of the heat flux distribution error as the integration rules change with different sets of 400 random “speckled” points in each cut element. However, when using  $p = 5$  polynomials to represent the solution, the heat flux distribution appears to be very dependent on the random sets of points. On the coarsest grid with  $p = 5$  the heat flux distribution error ranges from  $6.7 \times 10^{-2}$  to  $5.2 \times 10^{-5}$ .

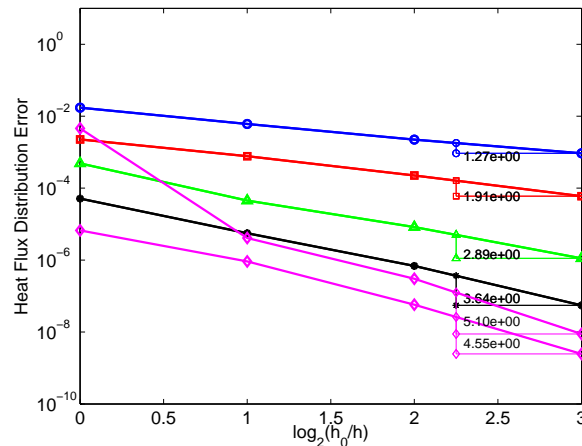


Figure 13. Convergence history of the minimum and maximum heat flux distribution error at solution orders 1 through 5, where a 100 different sets of “speckled” points are used for integration rules at the four grid refinement levels. Indicates that for solution orders 1 through 4 there is no variation in convergence as the “speckled” points randomly change. However at  $p = 5$  the convergence history has a wide range in the error.

Though the existence of a single cut mesh in a hundred with an order of magnitude worse heat flux distribution error is unsatisfactory, knowing the frequency of occurrence of the “bad” solutions is important. Figure 14 and Table 3 show the variation of the heat flux distribution error at  $p = 5$  for each of the four grid refinement levels. Figure 14 shows that the impact of randomness is strongest for the coarse grid. The coarse grid has one solution with a heat flux distribution error over eight hundred times higher than the minimum heat flux distribution error over the 100 sets of points examined. The impact of randomness is less apparent for the refined meshes. For the finer meshes the range of heat flux distribution error is only  $\mathcal{O}(10)$ . However, the differing error levels imply that a poor set of random numbers occurs too frequently and a new quadrature, or “speckling,” method is necessary to improve robustness.

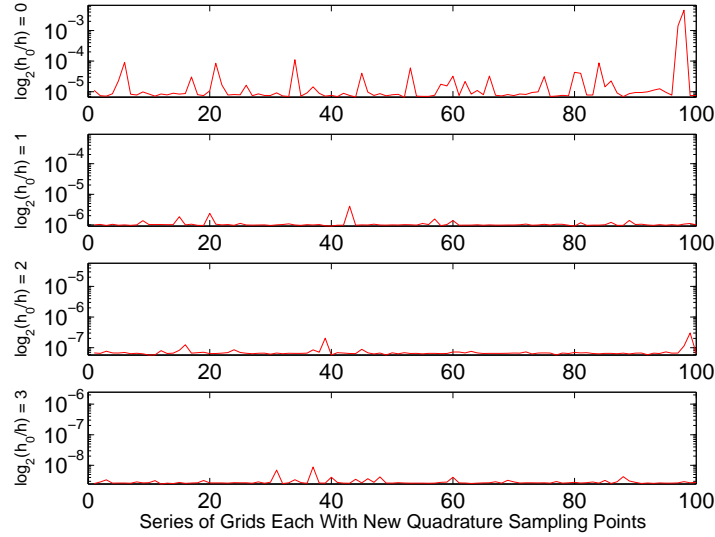


Figure 14. Range of heat flux distribution error over a 100 sets of “speckled” points at  $p = 5$  for each grid refinement level.

In order to increase the quality of the integration rules, canonical element shapes, Figure 11(b), can be recognized. In 2D, for example, essentially all cut elements have three or four sides. The primary exception to this is the element at a trailing edge which has two embedded surface faces cutting into it. However, three and four sided cut shapes can be mapped to triangles and quadrilaterals, respectively, to provide optimal integration rules in the reference space of the canonical element. It must be noted that the recognition of canonical shapes will be more difficult in three dimensions. In three dimensions the canonical options will not be simply tetrahedral and quadrilaterals. However, a similar canonical conversion process can be used. First cut-tetrahedral faces can be identified as triangles or quadrilaterals, then the resulting interior volumes can be recognized as a canonical object which is formed by a set of tetrahedrons. The proposed three-dimensional canonical conversion process simply requires meshing standard objects, like a tetrahedron with a node cut off, in linear reference space.

	$\frac{h_0}{h} = 1$	$\frac{h_0}{h} = 2$	$\frac{h_0}{h} = 4$	$\frac{h_0}{h} = 8$
Min HFDE over random sets	$6.66716 \times 10^{-6}$	$9.16533 \times 10^{-7}$	$5.74882 \times 10^{-8}$	$2.45837 \times 10^{-9}$
Max HFDE over random sets	$4.59215 \times 10^{-3}$	$4.11643 \times 10^{-6}$	$3.03729 \times 10^{-7}$	$8.83649 \times 10^{-9}$
Median HFDE over random sets	$4.81227 \times 10^{-4}$	$1.13621 \times 10^{-6}$	$7.69974 \times 10^{-8}$	$3.00955 \times 10^{-9}$
HFDE for canonical-cut grid	$8.02504 \times 10^{-6}$	$9.20516 \times 10^{-7}$	$5.75533 \times 10^{-8}$	$2.81036 \times 10^{-9}$

Table 3. Table comparing the minimum, maximum and median heat flux distribution errors over the 100 sets of randomly “speckled” sampling points to the heat flux distribution error from the same cut mesh with quadrature rules generated from canonical elements.

Cut elements are converted to canonical elements by using the higher-order geometry information from the faces of arbitrarily cut triangles or quadrilaterals to set the node locations on the element boundaries. Interior node locations are determined using a single element linear elasticity analogy using the location of the boundary nodes as Dirichlet conditions. A  $q = 5$  order Lagrange basis is used in this work to represent the geometry. Figure 11 visually shows the difference between the cut elements and the canonical elements. The figure also shows the required number of quad points for comparable accuracy between standard cut elements ( $N_{quad} = 400$ ) and cut elements which have been converted to canonical elements ( $N_{quad} = 40 - 64$ ). Along with a reduction in the number of quadrature points, the canonical element’s quadrature also comes with provable accuracy. Table 3 compares the integration rules generated from canonical elements to the rules generated from randomly “speckled” sampling points. The heat flux distribution error for the canonical

integration rules is close to the minimum heat flux distribution error over the 100 different sets of randomly “speckled” points.

Converting most cut elements to canonical elements also implies that for the remaining cut elements more “speckling” points or a more costly algorithm to for generating integration rules can be used. An increase in the number of sampling points tends to improve the integration rules and reduce variability. However, further improving the “speckling” method remains an area of continuing research.

#### IV. Solution Space

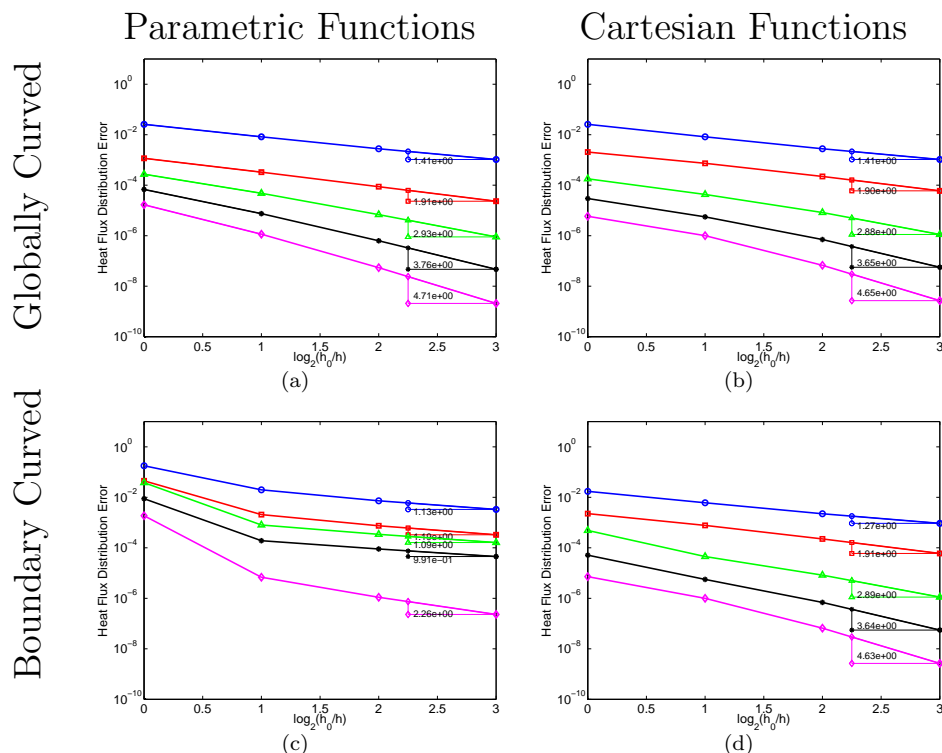


**Figure 15.** Comparison of the convergence in the heat flux distribution errors for cases with parametric and Cartesian approximation functions on globally curved higher-order meshes and globally linear meshes with a single curved boundary. The plots indicate that although there is a small deterioration in the error and rates with the Cartesian functions, the Cartesian functions still performs well at higher order even in linear meshes with a single higher-order surface.

In typical higher-order boundary-conforming meshes the solution approximation space is defined as polynomials on a reference element which is then mapped to the physical element. Mapping the solution approximation functions from reference space to physical space results in a parametric basis. The cut-cell method examined here depends on intersecting linear background meshes with higher-order embedded surfaces. The resulting cut elements can be arbitrarily shaped. Hence, a mapping from reference space to physical space is not guaranteed to exist and a parametric basis cannot be used for cut cells.

When using the DG finite element discretization and weakly enforced boundary conditions, another possibility besides parametric basis functions exists to approximate the solution. It is possible to associate a linear shadow element with each arbitrarily cut element and form a Cartesian basis. The Cartesian basis is generated using an affine mapping for the approximation functions from reference space to the shadow element. These Cartesian basis functions support solutions which are polynomial in physical space, i.e.  $x, y, xy, x^2, y^2, \dots$

This section examines the effect on solution efficiency (defined as accuracy per degree of freedom) of using a Cartesian basis compared to a parametric basis. To isolate the Cartesian and parametric bases their

comparison is performed without the inclusion of the cut-cell algorithm by comparing solutions on globally-curved meshes with linear boundary-curved meshes, Figure 12. Figure 15 shows the heat flux distribution error convergence comparison between parametric and Cartesian bases on both globally-curved meshes and boundary-curved meshes. Looking at the globally-curved mesh in isolation first, the Cartesian basis does result in slightly higher heat flux distribution errors and worse convergence rates in the asymptotic range, but the heat flux distribution errors on the initial grid for the Cartesian basis is actually better. Both bases result in essentially the same answer and can be used interchangeably for the globally-curved mesh without a loss of accuracy. Figure 15(c,d) shows the convergence of the heat flux distribution error on the boundary-curved mesh. For this mesh the Cartesian basis, Figure 15(d), performs significantly better than the parametric functions, Figure 15(c). In fact using the parametric functions with the boundary-curved mesh, Figure 15(c), results in both poor accuracy and low convergence rates. This implies that for cut elements that have been recognized as canonical shapes Cartesian bases should be used in place of parametric bases.

On Figure 15, an important comparison to make between a boundary-conforming method and a cut-cell method, is between the globally-curved case with parametric functions, Figure 15(a), and boundary-curved case with Cartesian functions, Figure 15(d). The boundary-curved Cartesian functions results in marginally inferior convergence rates compared to the globally-curved parametric basis. However, the difference in convergence rates does not lead to a significant discrepancy in accuracy between the globally-curved case with parametric functions and the boundary-curved case with Cartesian functions. The similarity in the accuracy of the two approximation functions is a significant conclusion for the cut-cell method, as it provides quantifiable evidence that high quality solutions can be generated with Cartesian approximation functions on arbitrarily cut elements.

## V. Output-Based Adaptation RANS Results

In this section results are presented from simulations of two-dimensional RANS flows using an output-based error estimation and cut-cell adaptation strategy. Variations of error estimation and adaptation strategies appear throughout the literature.<sup>2, 15, 26–29</sup> The implementation used here follows exactly the approach of Fidkowski and Darmofal.<sup>5, 15</sup> In this work an asymptotically dual-consistent discontinuous Galerkin discretization of the RANS equations with the Spalart-Allmaras (SA) turbulence model<sup>30, 31</sup> is used. Modifications to the original SA model based on the work of Oliver and Darmofal<sup>32–34</sup> are followed.

The three cases presented here are RANS simulations of a subsonic RAE2822, a transonic RAE2822, and a subsonic high-lift McDonnell Douglas Aerospace (MDA) three-element airfoil.

### V.A. Subsonic RAE2822

The first case of interest is  $M_\infty = 0.3$ ,  $Re_c = 6.5 \times 10^6$ ,  $\alpha = 2.31^\circ$ , turbulent flow over a RAE2822. The adaptation process begins with the coarse isotropic mesh shown in Figure 16. Figure 17 shows the adaptation history of the drag error indicator and the drag value. Once some level of grid refinement is reached, the benefit of the higher-order method is displayed as the  $p = 2$  and  $p = 3$  solutions reach lower error values at the same number of degrees of freedom compared to the  $p = 1$  solution. Also included in Figure 17 is the adaptation history for  $p = 1$  and  $p = 2$  boundary-conforming meshes. The boundary-conforming simulations were performed using the same flow solver and linear elasticity to convert linear boundary-conforming meshes to higher-order,  $q = 3$ , meshes. The comparison between boundary conforming and cut-cell meshes indicates that the boundary-conforming meshes can achieve lower error at a given degree of freedom count than the cut-cell method. The lower required degree of freedom for the same error is not unexpected. The boundary-conforming meshes have high aspect ratio curved elements on the geometry, where the cut-cell method has high aspect ratio linear elements which intersect the embedded boundary and get broken into a number of smaller elements. Though the boundary-conforming meshes outperform the cut-cell method for this simple geometry, mesh generation for the cut-cell method is significantly easier and therefore more automated.

Since pressure is an algebraic function of the state vector, it is relatively easy to resolve. Figure 18(a) reflects this fact as the pressure distributions for the final adaptive grids for  $p = 1, 2, 3$  are very smooth. Skin friction, on the other hand, is a derivative quantity and more prone to oscillations. Skin friction is therefore more sensitive to well conditioned bases and volume ratio. Figure 18(b) shows that, even though the drag error is quite low, oscillations remain in the skin friction. The oscillations are not unique to the cut-cell method as the final  $p = 2$  boundary conforming skin friction results also shown in Figure 18(b) contain

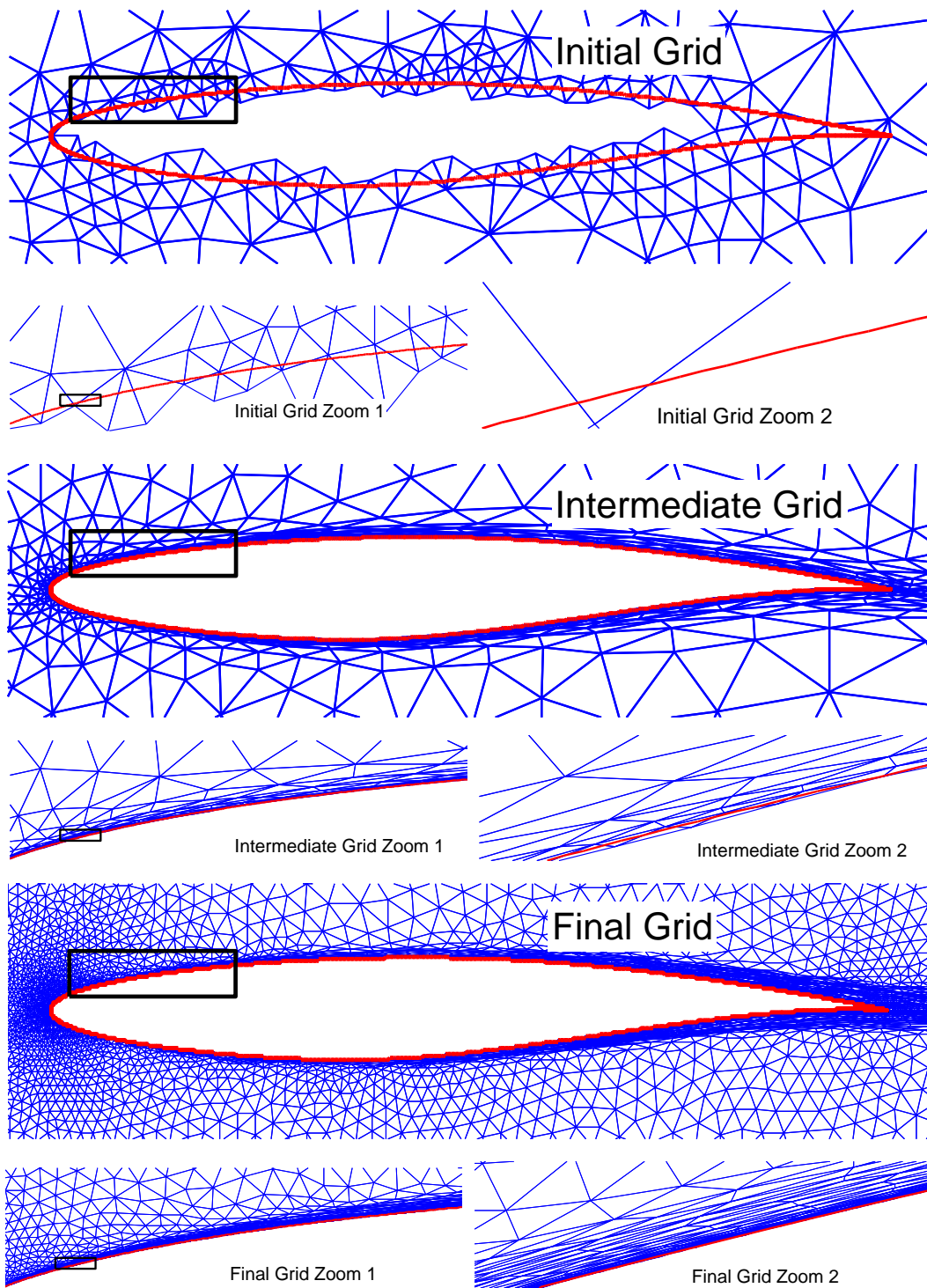
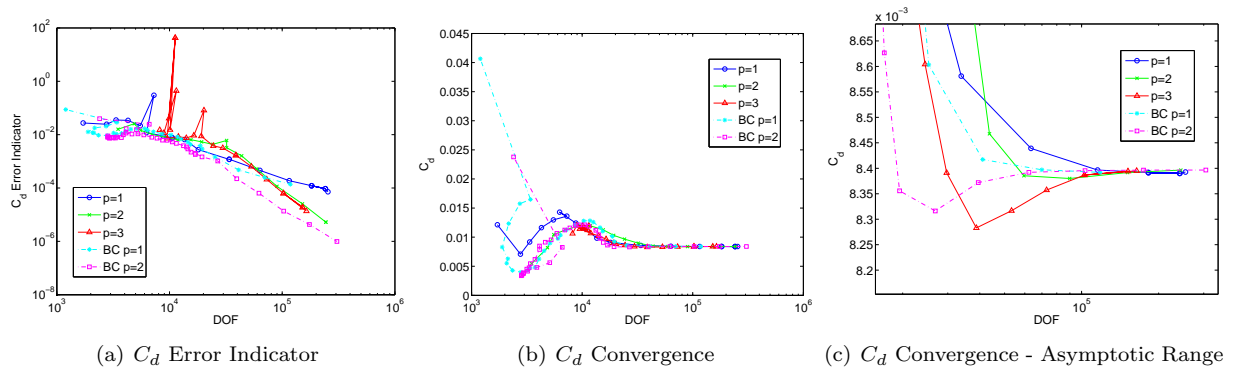
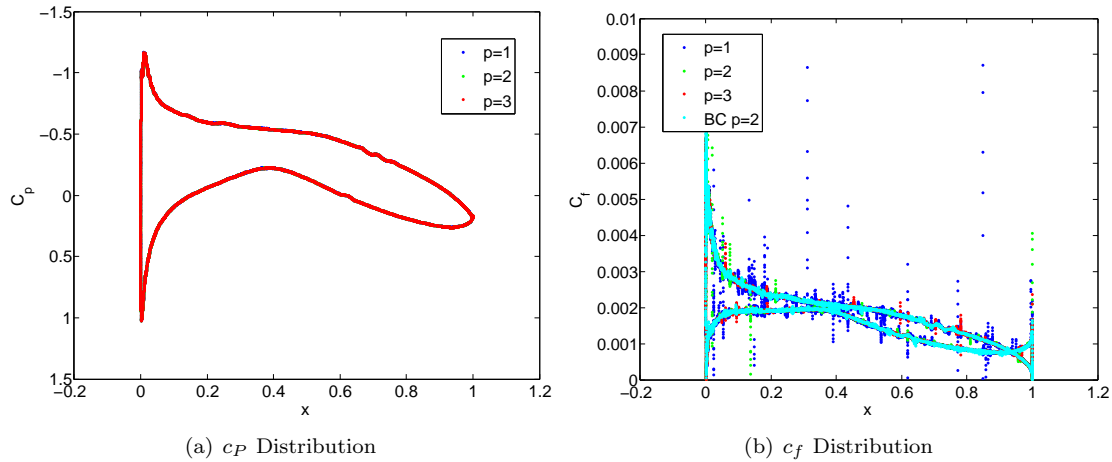


Figure 16. Initial, intermediate, and final mesh from the drag-based adaptation process for a  $p = 2$  solution for  $M_\infty = 0.3$ ,  $Re_c = 6.5 \times 10^6$ ,  $\alpha = 2.31^\circ$ , turbulent flow over a RAE2822.



**Figure 17.** Convergence plots for drag based error indicator and the drag itself versus degrees of freedom per state for  $M_\infty = 0.3$ ,  $Re_c = 6.5 \times 10^6$ ,  $\alpha = 2.31^\circ$ , turbulent flow over a RAE2822. Boundary-conforming mesh results are also included for comparison.

them. The skin friction results do however demonstrates the benefit of higher-order methods as the  $p = 3$  solution is much smoother than the lower-order solutions.



**Figure 18.** Surface distributions of  $c_p$  and  $c_f$  for  $M_\infty = 0.3$ ,  $Re_c = 6.5 \times 10^6$ ,  $\alpha = 2.31^\circ$ , turbulent flow over a RAE2822 for the final grids at  $p = 1, 2, 3$  solution orders. The small oscillations visible in the  $c_p$  distribution are a result of the RAE2822 geometry definition used and are not a result of the cut-cell method.

Figure 16 also shows an intermediate and the final mesh for  $p = 2$  adaptation process. The final mesh highlights the importance of the boundary layer for the turbulent flow.

## V.B. Transonic RAE2822

Next, a transonic case with shock boundary layer interaction is considered, where  $M_\infty = 0.729$ ,  $Re_c = 6.5 \times 10^6$ ,  $\alpha = 2.31^\circ$ . Shock capturing is performed using the PDE-based artificial viscosity model from Barter and Darmofal.<sup>35,36</sup> The adaptation process begins with the same initial mesh as used above for the subsonic RAE2822 and Figure 19 shows intermediate and final grids for  $p = 2$  solutions. The adaptation strategy has significantly more difficulty with the transonic RAE2822 compared to the subsonic case. The complication comes from accurately predicting the location of the shock. When the boundary layer is under-resolved the shock capturing scheme adds artificial viscosity that smooths the solution but also thickens the boundary layer. The thicker boundary layer causes the shock location to move forward. More adaptation iterations are needed compared to the subsonic case until the shock is in the correct location. The pressure

distribution in Figure 20(a) shows that the location of the shock matches well with experimental data from Cook et al.<sup>37</sup> Also the skin friction distribution in Figure 20(b) compares well with the cut-cell method providing a smooth distribution.

### V.C. Subsonic MDA Three Element Airfoil

The last test case considered is a high-lift MDA three element airfoil. The complex geometry of the three element airfoil is a good test of the robustness of the cut-cell method. Boundary-conforming meshes would be challenging to generate autonomously for this case even though it is only two-dimensional. Figure 21 shows the initial mesh used for the adaptation process. The initial isotropic mesh is very coarse containing 1046 elements and does not contain enough refinement for a satisfactory Euler solution. The turbulent flow conditions studied are  $M_\infty = 0.2$ ,  $Re_c = 9 \times 10^6$ , and  $\alpha = 8.1^\circ$ . Figure 22 shows the final adaptive grid. The final grid resolves the boundary layer with highly anisotropic elements. The resulting anisotropy emphasizes the benefit of the simplex cut-cell technique in that it is not something that could be generated with a Cartesian quadrilateral mesh.

Boundary distributions of pressure coefficient are shown in Figure 23. The adaptation process has successfully added sufficient resolution to the mesh for smooth surface pressure distributions.

## VI. Discussion and Conclusions

The goal of this work is to identify and resolve some of the limitations in the higher-order simplex cut-cell method. Sections II-IV detailed the three main limitations which have been observed in the cut-cell method. For each limitation, an approach was presented to resolve the issue.

An updated simplex cut-cell technique is demonstrated with the solution to high Reynolds number RANS simulation over complex geometries. For a transonic RAE2822, strong matching is seen between computation and experimental results. The utility of the cut-cell technique is demonstrated by the simulation of a three element airfoil. Future work will extend this approach to three dimensions.

## Acknowledgments

This work was supported by funding from The Boeing Company with technical monitor Dr. Mori Mani.

## References

- <sup>1</sup>Rannacher, R., "Adaptive Galerkin finite element methods for partial differential equations," *Journal of Computational and Applied Mathematics*, Vol. 128, 2001, pp. 205–233.
- <sup>2</sup>Giles, M. B. and Sili, E., "Adjoint methods for PDEs: a posteriori error analysis and postprocessing by duality," *Acta Numerica*, Vol. 11, 2002, pp. 145–236.
- <sup>3</sup>Venditti, D. A. and Darmofal, D. L., "Grid adaptation for functional outputs: application to two-dimensional inviscid flows," *Journal of Computational Physics*, Vol. 176, No. 1, 2002, pp. 40–39.
- <sup>4</sup>Park, M. A., "Adjoint-based, Three-dimensional Error Prediction and Grid Adaptation," *AIAA Journal*, Vol. 42, No. 9, 2004, pp. 1854–1862.
- <sup>5</sup>Fidkowski, K. J. and Darmofal, D. L., "Output-based adaptive meshing using triangular cut cells." M.I.T. Aerospace Computational Design Laboratory Report. ACDL TR-06-2, 2006.
- <sup>6</sup>Lee-Rausch, E. M., Park, M. A., Jones, W. T., Hammond, D. P., and Nielsen, E. J., "Application of Parallel Adjoint-Based Error Estimation and Anisotropic Grid Adaptation for Three-Dimensional Aerospace Configurations," AIAA Paper AIAA-2005-4842, 2005.
- <sup>7</sup>Jones, W. T., Nielsen, E. J., and Park, M. A., "Validation of 3D Adjoint Based Error Estimation and Mesh Adaptation for Sonic Boom Prediction," AIAA Paper 2006-1150, 2006.
- <sup>8</sup>Nemec, M., Aftosmis, M. J., and Wintzer, M., "Adjoint-Based Adaptive Mesh Refinement for Complex Geometries," AIAA Paper 2008-725, 2008.
- <sup>9</sup>Aftosmis, M. J., Berger, M. J., and Melton, J. M., "Adaptive Cartesian mesh generation," *Handbook of Grid Generation*, edited by J. F. Thompson, B. K. Soni, and N. P. Weatherill, CRC Press, 1998.
- <sup>10</sup>Aftosmis, M. J., "Solution Adaptive Cartesian Grid Methods for Aerodynamic Flows with Complex Geometries," *von Karman Institute for Fluid Dynamics, Lecture Series 1997-02*, Rhode-Saint-Genèse, Belgium, Mar. 3-7, 1997.
- <sup>11</sup>Nemec, M., Aftosmis, M., Murman, S., and Pulliam, T., "Adjoint formulation for an embedded-boundary Cartesian method," AIAA Paper 2005-0877, 2005.

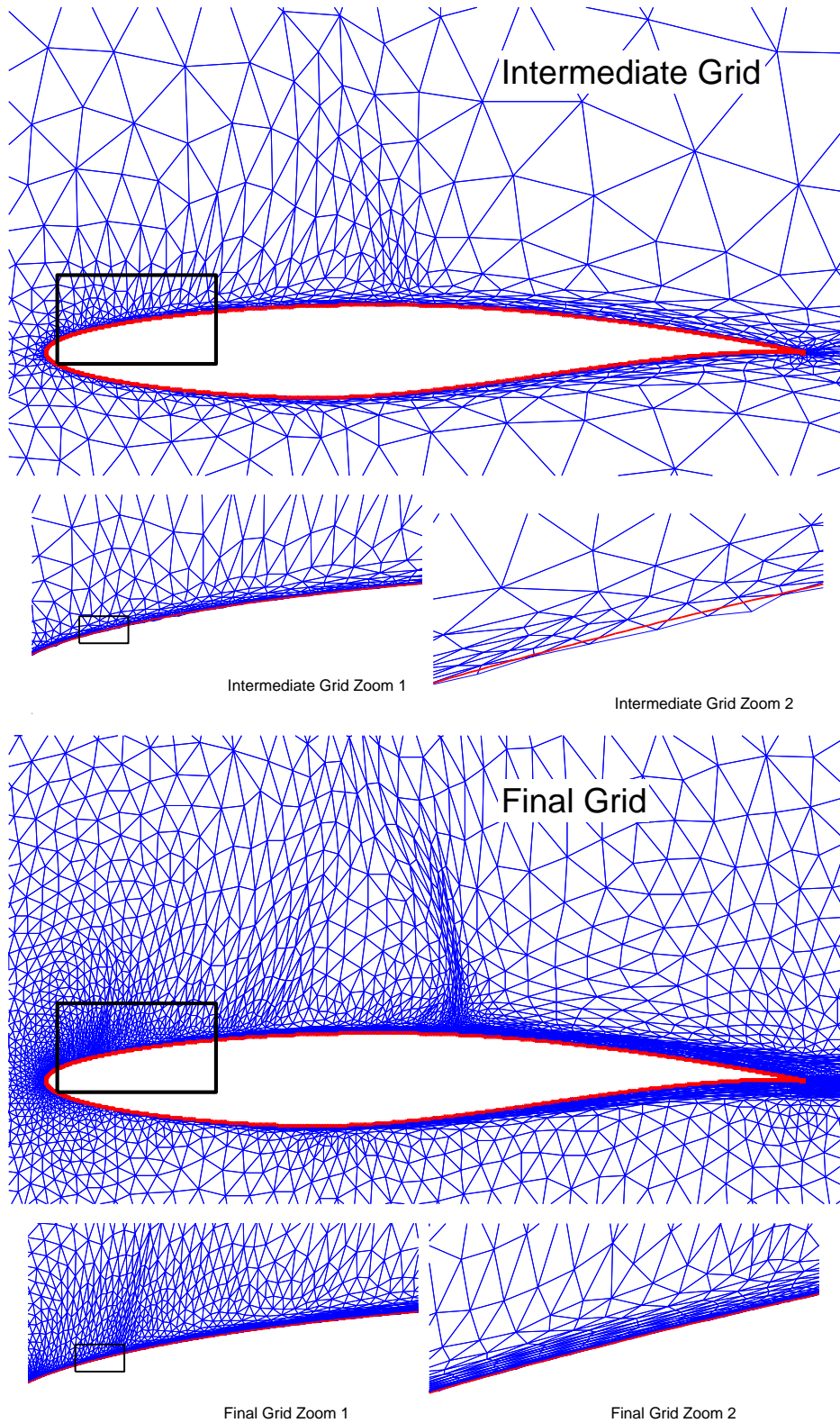


**Figure 19.** Initial, intermediate, and final mesh from the drag-based adaptation process for a  $p = 2$  solution for  $M_\infty = 0.729$ ,  $Re_c = 6.5 \times 10^6$ ,  $\alpha = 2.31^\circ$ , turbulent flow over a RAE2822.

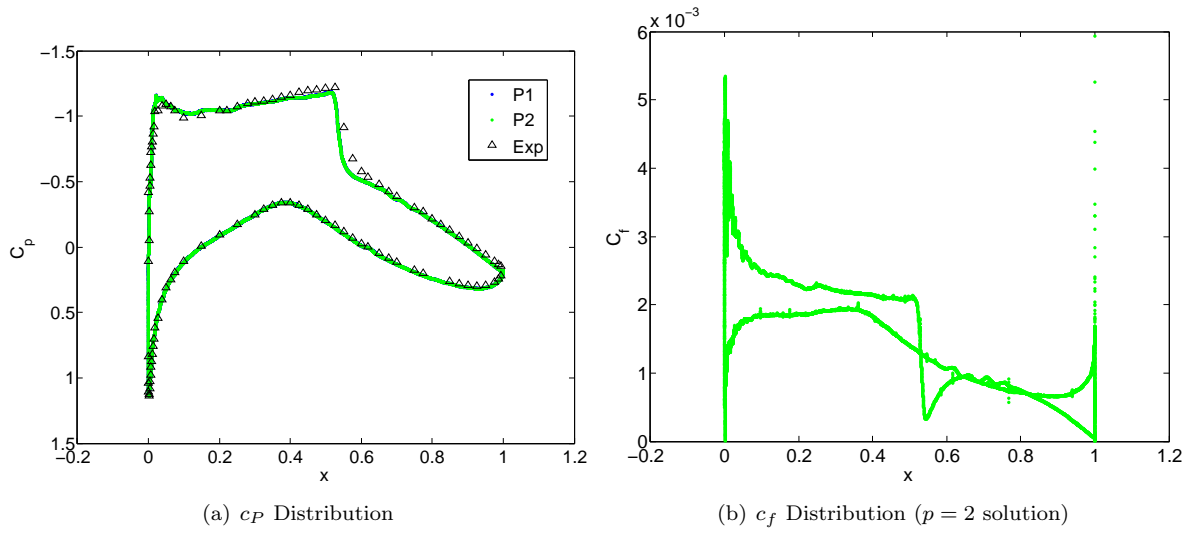


Figure 20. Surface distributions of  $c_p$  and  $c_f$  for  $M_\infty = 0.729$ ,  $Re_c = 6.5 \times 10^6$ ,  $\alpha = 2.31^\circ$ , turbulent flow over a RAE2822. Pressure distributions compared to experimental data from Cook et al.<sup>37</sup>

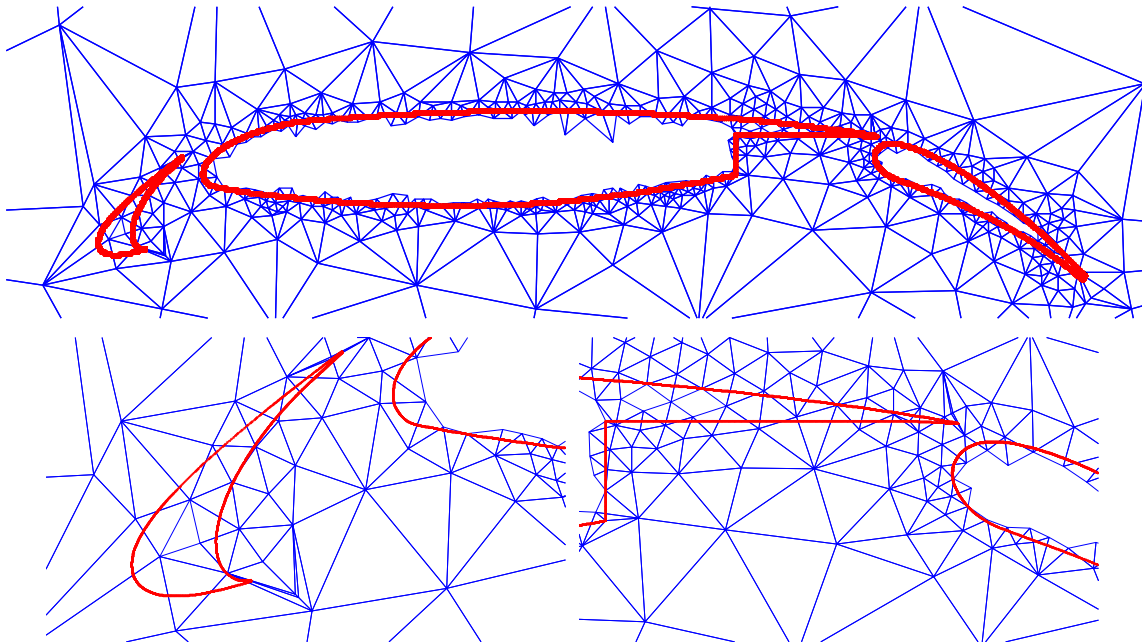


Figure 21. Initial mesh from the drag-based adaptation process for a  $p = 2$  solution for  $M_\infty = 0.2$ ,  $Re_c = 9 \times 10^6$ ,  $\alpha = 8.1^\circ$ , turbulent flow over an MDA three element airfoil.

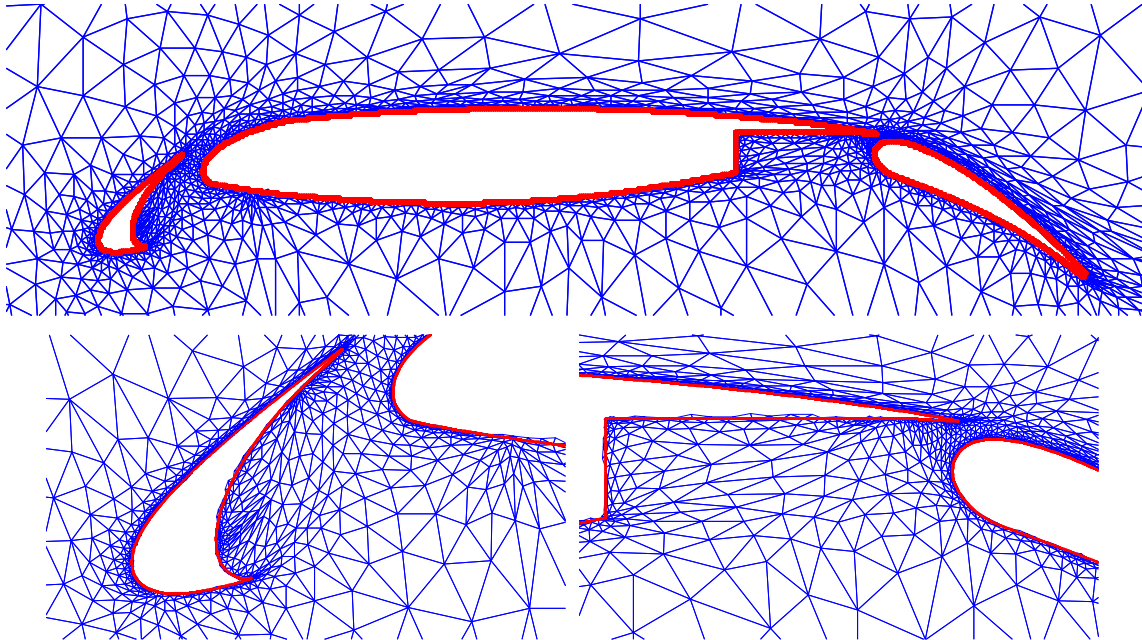


Figure 22. Final mesh from the drag-based adaptation process for a  $p = 2$  solution for  $M_\infty = 0.2$ ,  $Re_c = 9 \times 10^6$ ,  $\alpha = 8.1^\circ$ , turbulent flow over an MDA three element airfoil.

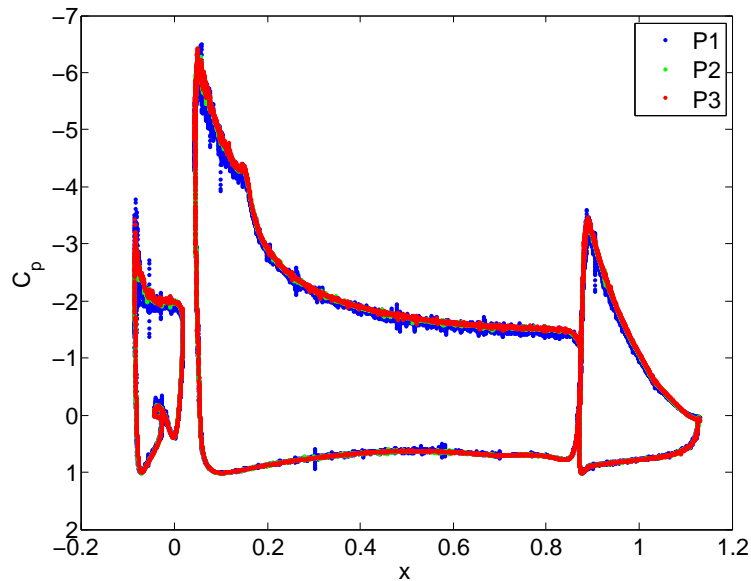


Figure 23. Surface pressure distributions for  $M_\infty = 0.2$ ,  $Re_c = 9 \times 10^6$ ,  $\alpha = 8.1^\circ$ , turbulent flow over an MDA three element airfoil.

- <sup>12</sup>Nemec, M. and Aftosmis, M. J., “Adjoint Error Estimation and Adaptive Refinement for Embedded-Boundary Cartesian Meshes,” AIAA Paper 2007-4187, 2007.
- <sup>13</sup>Fidkowski, K. and Darmofal, D., “An Adaptive Simplex Cut-Cell Method for Discontinuous Equations,” AIAA Paper 2007-3941, Massachusetts Institute of Technology, 2007.
- <sup>14</sup>Fidkowski, K. J. and Darmofal, D. L., “A Triangular Cut-Cell Adaptive Method for Higher-Order Discretizations of the Compressible Navier-Stokes Equations,” *Journal of Computational Physics*, Vol. 225, 2007, pp. 1653–1672.
- <sup>15</sup>Fidkowski, K. J., *A Simplex Cut-Cell Adaptive Method for High-Order Discretizations of the Compressible Navier-Stokes Equations*, PhD thesis, Massachusetts Institute of Technology, Department of Aeronautics and Astronautics, June 2007.
- <sup>16</sup>Cockburn, B. and Shu, C. W., “The Local Discontinuous Galerkin Method for Time-Dependent Convection-Diffusion Systems,” *SIAM J. Numer. Anal.*, Vol. 35, No. 6, December 1998, pp. 2440–2463.
- <sup>17</sup>Bassi, F. and Rebay, S., “High-order accurate discontinuous finite element solution of the 2D Euler equations,” *Journal of Computational Physics*, Vol. 138, No. 2, 1997, pp. 251–285.
- <sup>18</sup>Baumann, C. E. and Oden, J. T., “A Discontinuous  $hp$  Finite Element Method for the Euler and Navier-Stokes Equations,” *International Journal for Numerical Methods in Fluids*, Vol. 31, 1999, pp. 79–95.
- <sup>19</sup>Bassi, F. and Rebay, S., “GMRES Discontinuous Galerkin solution of the compressible Navier-Stokes equations,” *Discontinuous Galerkin Methods: Theory, Computation and Applications*, edited by K. Cockburn and Shu, Springer, Berlin, 2000, pp. 197–208.
- <sup>20</sup>Cockburn, B. and Shu, C.-W., “Runge-Kutta Discontinuous Galerkin methods for convection-dominated problems,” *Journal of Scientific Computing*, 2001, pp. 173–261.
- <sup>21</sup>Bassi, F., Crivellini, A., Rebay, S., and Savini, M., “Discontinuous Galerkin solution of the Reynolds averaged Navier-Stokes and  $k - \omega$  turbulence model equations,” *Computers and Fluids*, Vol. 34, May-June 2005, pp. 507–540.
- <sup>22</sup>Modisette, J. M. and Darmofal, D. L., “An Output-Based Adaptive and Higher-Order Method for a Rotor in Hover,” AIAA Paper 2008-7343, 2008.
- <sup>23</sup>Gaffney, R. L., Hassan, H. A., and Salas, M. D., “Euler Calculations for Wings Using Cartesian Grids,” AIAA Paper 87-0356, Jan 1987.
- <sup>24</sup>Clarke, D. K., Salas, M. D., and Hassan, H. A., “Euler Calculations for Multielement Airfoils Using Cartesian Grids,” *AIAA Journal*, Vol. 24, No. 3, 1986, pp. 353–358.
- <sup>25</sup>Diosady, L. T. and Darmofal, D. L., “Preconditioning methods for discontinuous Galerkin solutions of the Navier-Stokes equations,” *Journal of Computational Physics*, 2009, pp. 3917–3935.
- <sup>26</sup>Becker, R. and Rannacher, R., “An optimal control approach to a posteriori error estimation in finite element methods,” *Acta Numerica*, edited by A. Iserles, Cambridge University Press, 2001.
- <sup>27</sup>Venditti, D. A. and Darmofal, D. L., “Anisotropic grid adaptation for functional outputs: application to two-dimensional viscous flows,” *Journal of Computational Physics*, Vol. 187, No. 1, 2003, pp. 22–46.
- <sup>28</sup>Lu, J., *An a Posteriori Error Control Framework for Adaptive Precision Optimization Using Discontinuous Galerkin Finite Element Method*, Ph.D. thesis, Massachusetts Institute of Technology, Cambridge, Massachusetts, 2005.
- <sup>29</sup>Hartmann, R. and Houston, P., “Adaptive discontinuous Galerkin finite element methods for the compressible Euler equations,” *Journal of Computational Physics*, Vol. 183, No. 2, 2002, pp. 508–532.
- <sup>30</sup>Spalart, P. R. and Allmaras, S. R., “A One-Equation Turbulence Model for Aerodynamics Flows,” , No. 1992-0439, Jan. 1992.
- <sup>31</sup>Spalart, P. R. and Allmaras, S. R., “A One-Equation Turbulence Model for Aerodynamics Flows,” *La Recherche Aéropatiale*, Vol. 1, 1994, pp. 5–21.
- <sup>32</sup>Oliver, T. A., *Multigrid Solution for High-Order Discontinuous Galerkin Discretizations of the Compressible Navier-Stokes Equations*, Masters thesis, Massachusetts Institute of Technology, Department of Aeronautics and Astronautics, June 2004.
- <sup>33</sup>Oliver, T. A., *A Higher-Order, Adaptive, Discontinuous Galerkin Finite Element Method for the Reynolds-Averaged Navier-Stokes Equations*, PhD thesis, Massachusetts Institute of Technology, Department of Aeronautics and Astronautics, June 2008.
- <sup>34</sup>Oliver, T. and Darmofal, D., “Impact of Trubulence Model Irregularity on High-Order Discretizations,” AIAA Paper 2009-953, 2009.
- <sup>35</sup>Barter, G. E., *Shock Capturing with PDE-Based Artificial Viscosity for an Adaptive, Higher-Order, Discontinuous Galerkin Finite Element Method*, PhD thesis, Massachusetts Institute of Technology, Department of Aeronautics and Astronautics, June 2008.
- <sup>36</sup>Barter, G. and Darmofal, D., “Shock Capturing with Higher-order, PDE-Based Artificial Viscosity,” AIAA Paper 2007-3823, 2007.
- <sup>37</sup>Cook, P. H., McDonald, M. A., and Firmin, M. C. P., “Aerofoil RAE 2822 - Pressure Distributions, and Boundary Layer and Wake Measurements,” *AGARD Report*, , No. 138, 1979.